Petroleum Science 21 (2024) 2881–2891

Contents lists available at ScienceDirect

Petroleum Science

journal homepage: www.keaipublishing.com/en/journals/petroleum-science

Original Paper

Regulating metal-acid double site balance on mesoporous SiO_2-Al_2O_3 composite oxide for supercritical *n*-decane cracking

Liu-Ling Chen [a], Jun Zhang [c, d], Chun-Guang Li [b], Li-Qun Fei [b], Bo Wang [c], Chen-Qi Zhang [c], Yi Jiao [a, *], Jian-Li Wang [a, c]

[a] Institute of New Energy and Low-Carbon Technology, Sichuan University, Chengdu, 610064, Sichuan, China
[b] Science and Technology on Scramjet Laboratory, Beijing Power Machinery Research Institute, Beijing, 100074, China
[c] Engineering Research Center of Combustion and Cooling for Aerospace Power, Ministry of Education, School of Chemical Engineering, Sichuan University, Chengdu, 610064, Sichuan, China
[d] State Key Laboratory of Industrial Vent Gas Reuse, Southwest Institute of Chemical Co., Ltd, Chengdu, 610065, Sichuan, China

ARTICLE INFO

Article history:
Received 31 October 2023
Received in revised form
27 November 2023
Accepted 3 February 2024
Available online 15 February 2024

Edited by Min Li

Keywords:
Metal-acid dual sites balance
Catalytic cracking
Hydrocarbon fuels
Chemical heat sink
Carbon deposition

ABSTRACT

The balance between metal and acid sites directly affects the preparation of high-performance cracking catalysts with high heat sink and low coking. Nevertheless, how to control acid-metal sites balance and its relationship with cracking performance are reported scarcely. In this work, a series of Pt/Al_2O_3-SiO_2 dual sites catalysts with different metal to acid active sites ratio (C_M/C_{SA}) were constructed by ethanol-assisted impregnation method and the impact on *n*-decane cracking under supercritical conditions was systematically and deeply investigated. The results showed that the conversion and carbon deposition increased gradually with varied C_M/C_{SA} and reached the balance at C_M/C_{SA} of 0.13. The proper ratio C_M/C_{SA} (0.13) can balance the deep dehydrogenation coking over metal active sites and high heat sink of cracking over acid active sites, the chemical heat sink reaches amazing 1.75 MJ/kg and carbon deposition is only 22.03 mg/cm^2 at 750 °C. Meanwhile, the few metal sites at low C_M/C_{SA} and the few strong acid sites at high C_M/C_{SA} are the main factors limiting the cracking activity. Low C_M/C_{SA} limit the activation of C—H bond and deep dehydrogenation of coking precursor, resulting in relative low cracking activity and carbon deposition, while high C_M/C_{SA} limit the activation of C—C bond and increase the deep dehydrogenation. In this contribution, design and construction of metal-acid dual sites can not only provide the technical solution for the preparation of high heat sink and low coking cracking catalyst, but also deepen the understanding of the cracking path of hydrocarbon fuel.

1. Introduction

Supersonic vehicles cruising at Mach 5 or higher speed is subjected to the tremendous aerodynamic and combustion heat that exceeds the suffertibility of structure materials (Zhu et al., 2018; Tian et al., 2021; Feng et al., 2020). In this case, on-board endothermic hydrocarbon fuels (EHFs) acting as propellant and coolant circulate in the parallel cooling microchannel on the wall of airframe to absorb the excess heat (Shang et al., 2019). Simultaneously, EHFs crack into low-carbon olefins and hydrogen to improve the combustion efficiency (Song et al., 2020). In order to achieve higher speed and longer period of flight, higher heat sink (heat absorption capacity) and lower carbon deposition are required during the cracking process. Higher heat sink derives from high conversion and olefin selectivity during EHFs cracking, but it inevitably leads to produce more carbon deposition. The contradiction between high heat sink and low carbon deposition in the cracking process has been the research focus. Catalytic cracking can regulate the reaction pathway via adjusting the intrinsic properties of catalyst, such as acid and metal sites, then enhance the chemical heat sink as well as decrease carbon deposition, so that it attracts a great deal of attention (F.Q. Chen et al., 2022; K. Chen et al., 2022; Xiao et al., 2022).

C—C bond of EHFs is activated on the strong acid sites to form highly reactive carbenium ion intermediates, ulteriorly crack into smaller hydrocarbon (Hou et al., 2017a). Solid acid catalysts, such as

* Corresponding author.
E-mail address: jiaoyiscu@163.com (Y. Jiao).

https://doi.org/10.1016/j.petsci.2024.02.005

zeolites and acid oxides, were widely used for catalytic cracking of EHFs owing to the strong and adjustable surface acidity (Dong et al., 2018). Wang et al. (2017) investigated the cracking of methylcyclohexane over different acidic amorphous SiO_2-Al_2O_3 composites, and found that the heat sink over Rh/60% SiO_2-Al_2O_3 at 675 °C reached 3.09 MJ/kg due to strong Lewis acid sites. He et al. (2023) synthesized ZSM-5 with high acid density to improve *n*-pentane cracking conversion and modified the acidic characteristic to increase the light olefins selectivity. Although the reaction pathway can be controlled through the regulation of acidity to improve chemical heat sink, more carbon deposition can be generated uncontrollably, covering the active site and shortening the catalyst life. Incorporation of active metals, such as Gd, Co, Ni, Ag, Pd, Au, Pt, etc. (Long et al., 2020; Kim et al., 2015; Hou et al., 2017b; Ye et al., 2019) to form dual sites catalysts is deemed to effectively heighten the cracking heat sink, olefin selectivity and decrease carbon deposition. Hou et al. (2017b) have reported that the regenerated Ag-ZSM-5 for *n*-pentane cracking reached 69% olefines selectivity, being higher than ZSM-5 (55%) due to appearance of new metal site (Ag species) and lowered apparent activation energy for breakage of C—H bond. Ye et al. (2019) have investigated the enhancement effects of metal sites (Pt, Pd, Au) in EHF (decalin) cracking, especially Pt at 675 °C, in terms of decalin conversion (22.3—50.7%), heat sink (2.18—2.62 MJ/kg) and olefins selectivity. Hence, the role of metal incorporation in EHFs cracking can be ascribed to dehydrogenation active sites, which boost the fracture of C—H bond (Hou et al., 2018). Kim et al. (2015) have reported that the Gd can increase the Lewis acid sites of ZSM-5 zeolite and inhibit the formation of complex aromatic coke. Although the synergistic catalysis of metal sites and acid sites could improve the heat sink and conversion, some unfavorable effects still exist in dual sites catalysts for EHFs cracking (Kim et al., 2015; Musselwhite et al., 2015): (a) the side reactions to produce carbon deposition, such as cyclization, aromatization and oligomerization, etc., would take place at excess strong acid sites; (b) the alkenes generated by dehydrogenation of alkanes on metal sites may be adsorbed by acid sites and polymerize to form coking precursors; (c) alternatively, the olefins produced by β-scission on the acid sites are adsorbed by the metal sites and further dehydrogenated to produce coke. In short, excess acid sites or metal sites would result in carbon deposition, and increase of metal loading will would contribute to sintering. Accordingly, to solve the conflict between high heat sink and carbon deposition of *n*-decane cracking over metal-acid dual sites catalysts and make full use of dual sites, it is necessary to regulate the balance between acid and metal sites on the prerequisite of appropriate amount of acid site.

Many researches have also reported the coordinated regulation of metal-acid dual sites and effect of metal-acid sites balance on hydrocarbon isomerization (Mendes et al., 2020; Samad et al., 2016). Wang et al. (2019) have reviewed the effect of metal-acid dual sites balance on isomerization of *n*-alkanes, claiming that ideal balance is beneficial for improving the function of metal sites as well as lowering the cost of preparation. Lyu et al. (2019) have studied metal-acid dual sites balance in forms of variation of metal to acid sites ratio (C_M/C_A) over Ni/SAPO-11 via changing the additive amount of Ni, found that turnover frequency increased with C_M/C_A until a plateau ($C_M/C_A \approx 0.19$). Samad et al. (2016) have prepared a series Pt/Al-Si dual sites catalysts with wide C_M/C_A for *n*-heptane isomerization via varying content of Pt. From the above, a simple approach to control C_M/C_A of dual sites catalyst is loading different content of metal (Musselwhite et al., 2015). Metal-acid sites balance in dual sites catalysts have been reported in researches of hydrocarbon isomerization, but the regulation of dual sites high-performance catalysts and the impact of dual sites balance on supercritical cracking have been studied scarcely. Here, typical acidic oxides (SiO_2-Al_2O_3) was selected to load varying content of Pt by impregnation method using ethanol as solvent, which can alleviate the influence of impregnation process on certain properties of support. Thus, a series of dual sites catalysts with different C_M/C_A were successfully prepared and characterized. Meanwhile, the impact of metal-acid dual sites balance on catalytic cracking of EHF in microchannel reactor was investigated over these catalysts. The correlation between metal-acid sites balance (C_M/C_A) and catalytic cracking performance, in the forms of the heat sink, gas yield and carbon deposition, was established. Moreover, cracking reaction pathway was also analyzed, this study may shed new light on designing highly active dual sites cracking catalysts and the better comprehension for metal-acid sites balance.

2. Materials and methods

2.1. Catalyst and coating preparation

Ethanol was chosen as the solvent in view of its weak surface tension and better reducing properties, which can effectively promote the dispersion of particles. Various content of Pt, including 0.35, 0.71, 1.0, 1.5 and 2.0 wt%, loaded onto 30 wt% SiO_2-Al_2O_3 support by incipient-wetness impregnation method were denoted as $P_{0.35}$Al-Si, $P_{0.71}$Al-Si, $P_{1.0}$Al-Si, $P_{1.5}$Al-Si and $P_{2.0}$Al-Si, respectively. In a typical process, 12 g SiO_2-Al_2O_3 powder was added into Pt precursor [Pt $(NO_3)_2 \cdot 6H_2O$] ethanol solution with continuous 30 min stirring at room temperature (RT). The obtained catalyst stood for the overnight at RT, then water bath at gradient temperature (50, 70, 90 and 120 °C), finally the powder was calcined at 550 °C for 3 h. More details of reagent used were presented in Supplementary Materials.

Catalyst coating in microchannel reactor was prepared by wash-coating method in our previous work (Zhang et al., 2021) using inorganic adhesive without catalytic activity. The length and inner diameter (I.D.) of the stainless-steel reaction tubes (SUS 316 L) are 800 and 2 mm, respectively. Catalyst weight on each reaction tube is 0.2 ± 0.02 g. As-obtained coating was reduced at 600 °C for 1 h under H_2 flow, then ultrasonic oscillation test was performed to ensure that the shedding rate is less than 2%.

2.2. Catalyst characterization

The physiochemical properties of catalysts were characterized by multiple characterization techniques. Textural properties, BET surface area (S_{BET}), total pore volume (V_{total}) and mean pore radius (R_m) were measured by N_2 adsorption-desorption. Crystal states of catalysts were detected by X-ray diffraction (XRD). The practical metal loading is determined by X-ray fluorescence (XRF). X-ray photoelectron spectroscopy was applied to investigate the chemical state of Pt and content of surface elements according to bind energy of Pt 4d5/2 and corresponding area. Content of reducible Pt over catalysts was obtained by H_2 temperature programmed reduction (H_2-TPR). Particle size and dispersive state of Pt metal over the catalysts were acquired by transmission electron microscopy (TEM). The accessible Pt metal sites (C_M) of catalysts were studied via CO chemisorption after reduction. Meantime, the states of CO chemisorbed on metallic Pt were investigated by Fourier transform infrared spectroscopy using CO as probe molecule (CO-DRIFTS). The number and distribution of acid sites were determined by NH_3 temperature programmed desorption (NH_3-TPD). The Brønsted and Lewis acid sites of catalysts were measured by *in situ* DRIFTS of adsorbed NH_3. In addition, the number of active acid sites (C_A) is defined as the number of strong acid site because only it boosts hydrocarbon fuel cracking. Experimental details of characterizations were described in Supplementary Materials.

2.3. Catalytic reaction test

Catalytic cracking of *n*-decane was carried on the tubular reactor under supercritical conditions (3.5 MPa and above 345 °C). Prior to the test, N_2 (99.99%) purges the system for removing oxygen and residual fuel. As shown in Fig. S1, *n*-decane (1.0 g/s) is pumped into system via high pressure constant flow pump. The fuel flowing through preheat section is heated to 450 °C by AC transformer (metal tube as heating resistance), then enters the microchannel reactor with catalytic coating and fuel temperature was controlled at 600–750 °C with interval of 50 °C. The cracking products of different temperature point was cooled through water-condenser then separated into liquid and gaseous products that were analyzed by gas chromatography (PerkinElmer, Germany); The liquid phase products flowed out of the bottom end, and the liquid phase products were collected for 3 min at each temperature point and weighed to calculate the gas yield. Average amount as well as oxidizability of coke was obtained by temperature programmed oxidation (TPO) using an IR detector. Specific analysis conditions were presented in Supplementary Material. Catalytic cracking performance, in the forms of chemical heat sink (H_c, MJ/kg), gas yield (X_d, %) and average amount of coke ($\overline{M_c}$, mg/cm^2) were calculated by following equations, Eq. (1), Eq. (2) and Eq. (3), severally.

$$H_c = H_s - H_p = \frac{P_{out} - P_{loss}}{q_m} - Hp = \frac{UI - P_{loss}}{q_m} - H_p \quad (1)$$

$$X_d = \frac{q_m - R_m}{q_m} \times 100\% \quad (2)$$

$$\overline{M}_c = \frac{m_c}{A_i} = \frac{m_c}{\pi dL} \quad (3)$$

wherein, H_s is total heat sink, P_{out} is output power (W), P_{loss} is power loss (W) and obtained without fluid, U is alternating voltage (V), I is alternating current (A), q_m is mass flow rate (g/s), H_p is physical heat sink (MJ/kg). R_m is cracking residual liquid (g/s), m_c is mass of coke (g), d is I.D. of reactor (2 mm) and L is last 50 mm of reactor.

In order to guarantee the repetition of experimental results, each catalyst was evaluated under same conditions at least twice with relative error less than 3% and the average value was presented in this work. Meanwhile, Table S2 listed the uncertainty of the data measurement process. In addition, the fitting and calculation of the heat loss is shown in the Supplementary Materials.

3. Results and discussion

3.1. Influence of Pt loading on structure and morphology

The $P_{0.35}$Al-Si, $P_{0.71}$Al-Si, $P_{1.0}$Al-Si, $P_{1.5}$Al-Si and $P_{2.0}$Al-Si catalysts are synthesized by loading different Pt content, and the actual Pt content is listed in Table 1. Obviously, the Pt content of the catalysts is consistent with the design value. In order to prove that the textural properties were affected rarely by ethanol-assisted impregnation method, N_2 adsorption-desorption isotherms and pore size distribution of SiO_2-Al_2O_3 are tested and shown in Fig. 1(a) and (b). All the isotherms presented type IV isotherms with same hysteresis loop (type H3) according to the IUPAC classification and the most probable pore diameter concentrated upon about 4 nm. The BET specific surface area (S_{BET}), total pore volume (V_{total}) and average pore radius (R_m) for these catalysts are summarized in Table 1. There are minor changes in these parameters, indicating that the addition content of active metal Pt did not significantly influence the textural properties of support. Moreover, the S_{BET} and V_{total} are larger than 150 m^2/g and 0.4 cm^3/g, respectively, which can provide enough place for cracking reaction. Fig. 1(c) displayed the crystal structure of catalysts. The 2θ values located at 39.8°, 46.2° and 67.4° are attributed to characteristic peaks of Pt (111), (200) and (220) crystal faces (Zhang et al., 2021). Pt (200) and (220) characteristic peaks overlap with two peaks (JCPDS 77-0396) of Al_2O_3. The relative intensity of Pt (111), thus, is calculated, as presented in Fig. 1(c1). Apparently, there is a surge of the relative intensity when Pt loading content is 1.5 wt%. Correspondingly, it can be seen from Fig. 1(d) that Pt uniformly dispersed on the $P_{0.35}$Al-Si, $P_{0.71}$Al-Si and $P_{1.0}$Al-Si, while obvious Pt particle aggregation occurs on the surface of $P_{1.5}$Al-Si and $P_{2.0}$Al-Si catalysts. The particle size distribution of each catalyst was estimated by measuring at least 300 Pt particles from TEM images, as depicted in Fig. 1(d). As well, the average Pt particle size is fitted to be 1.70 ± 0.42, 1.71 ± 0.57, 2.04 ± 0.48, 2.27 ± 0.52 and 3.10 ± 0.75 nm, ascribing to $P_{0.35}$Al-Si, $P_{0.71}$Al-Si, $P_{1.0}$Al-Si, $P_{1.5}$Al-Si and $P_{2.0}$Al-Si catalysts, respectively. The Pt dispersion determined by CO chemisorption was calculated with assumptions that one accessible Pt sites can adsorb one CO molecule (Lee et al., 2017). Pt dispersion dropped with Pt loading: $P_{0.35}$Al-Si (40.0%) > $P_{0.71}$ Al-Si (38.2%) > $P_{1.0}$Al-Si (35.2%) > $P_{1.5}$ Al-Si (32.1%) > $P_{2.0}$ Al-Si (29.9%). Apparently, Pt particle size grew while dispersion decline with the Pt loading content increase.

3.2. Metal active sites (Pt NPs) over catalysts

Catalytic cracking activity of supported catalysts normally relies on geometry, electronic state and the number of active Pt sites. HAADF, EDX mapping and HRTEM of $P_{0.71}$Al-Si catalyst were implanted in Fig. 2(a). Obviously, the Pt dispersed on the support equably. The lattice fringe spacing of 2.26 Å is indexed as the exposed Pt (111) facet. The Pt nanoparticles (NPs) shows a distinct hexagon profile, corresponding to cuboctahedron structure of Pt NPs, which was also observed in the other research (Tuo et al., 2021; Chen et al., 2020). The Pt NPs geometrical structures include cuboctahedron, cube, sphere and truncated octahedron, as well as the particle geometry hardly impact the concentration of sites (Kale and Christopher, 2016). Due to symmetrical structure of cuboctahedron, CO molecule adsorbed on the half is schematically shown in Fig. 2(b). Cuboctahedron shape model contains Pt (111)

Table 1
Textural parameters, actual Pt content, particle size for catalysts.

Catalysts	Actual Pt content[a], wt%	S_{BET}, m^2/g	V_{total}, cm^3/g	R_m, nm	Particle size[b], nm	Pt dispersion, %
$P_{0.35}$Al-Si	0.353	152.8	0.495	5.48	1.70	40.0%
$P_{0.71}$Al-Si	0.720	158.3	0.460	5.81	1.71	38.2%
$P_{1.0}$Al-Si	1.007	158.9	0.429	5.39	2.04	35.2%
$P_{1.5}$Al-Si	1.536	157.9	0.457	5.78	2.27	32.1%
$P_{2.0}$Al-Si	2.083	160.5	0.451	5.62	3.10	29.9%

[a] Determined by XRF.
[b] Obtained by TEM.

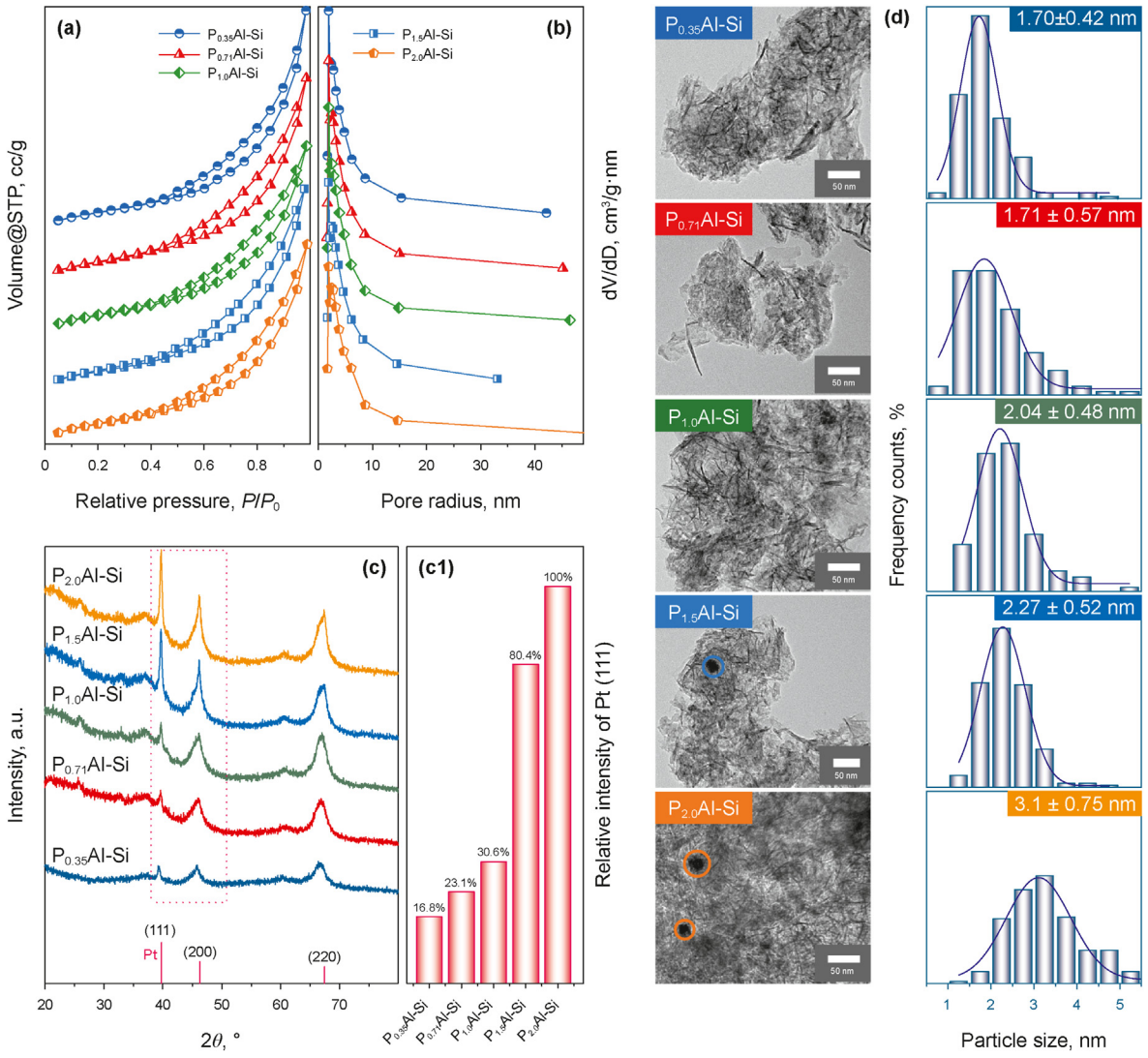

Fig. 1. **(a)** N_2 adsorption-desorption isotherms of Pt/Al-Si catalysts. **(b)** Pore size distribution of catalysts. **(c)** XRD patterns of $P_{0.35}$Al-Si, $P_{0.71}$Al-Si, $P_{1.0}$Al-Si, $P_{1.5}$Al-Si and $P_{2.0}$Al-Si catalysts. **(d)** TEM images and corresponding Pt particle size distributions.

(9-fold coordination) and (100) (8-fold coordination) terrace atoms corresponding to well-coordinated sites (WC) as well as edges (7-fold coordination) and corner (6-fold coordination) atoms combined to under-coordinated sites (UC) (McCarthy et al., 2012). Meantime, the CO adsorbed on different active sites would display disparate vibration stretch frequency. The chemical state of Pt NPs on the catalysts, therefore, was determined by CO-DRIFTS at the range from 2000 to 2100 cm^{-1} (Fig. 2(c)). The peak can be deconvoluted into three peaks at 2081, 2072 and 2048 cm^{-1}, corresponding to collective oscillation of CO molecule linearly adsorbed on the WC, UC and highly under-coordination (UC) sites, respectively (Lundwall et al., 2010). Firstly, the amount of CO adsorbed increases gradually due to more active Pt active sites, being consistent with CO chemisorption results. Secondly, the fraction of WC sites (at 2081 cm^{-1}) rises with the Pt loading, this may be closely relative to growing Pt particle size (Sun et al., 2021) and intensity variation for characteristic peak of Pt (111) plane in XRD results proved this. In the research (Hammer et al., 1997), because of more charge transfer to CO from Pt UC sites, the adsorption energy of CO on the Pt UC sites is 0.5–1.0 eV higher than that on WC sites. Meantime, Ludwig et al. (2006) have reported that the coordination unsaturated step sites (UC) in contrast to terrace sites (WC) are in favor of dissociation of Hydrogen, according to ReaxFF results. Namely, the hydrogen production is more toilless on the UC sites rather on the WC sites during the cracking (Sun et al., 2021). Thus, different ratio of UC sites on the catalyst will lead to the difference of dehydrogenation activity.

To clarify the interaction between metal Pt active sites and support, H_2-TPR technology was employed, as shown in Fig. 2(d). For each curve, an obvious peaks are presented centralized at 228 °C, which belong to reduction of PtO_x to Pt. The reduction peak can be resolved into three peaks, as shown in Fig. S2 (for $P_{0.35}$Al-Si), indicating dissociative, weak interacted and strong interacted PtO_x species, respectively. However, reduction peak temperature over each catalyst shifts scarcely, suggesting that only the subtle difference of interaction between reducible PtO_x and support for these catalysts exists. Thus, XPS characterization of Pt/Al-Si catalysts was executed to further demonstrated the electronic state of Pt species on the surface of catalyst with different Pt loading content. The XPS characteristic peak of Pt is Pt 4f, but the corresponding bind energy region was covered by the characteristic peak (Al 2p, 70–78 eV) of Al. Here, photoemission line of Pt 4d5/2 was detected and depicted

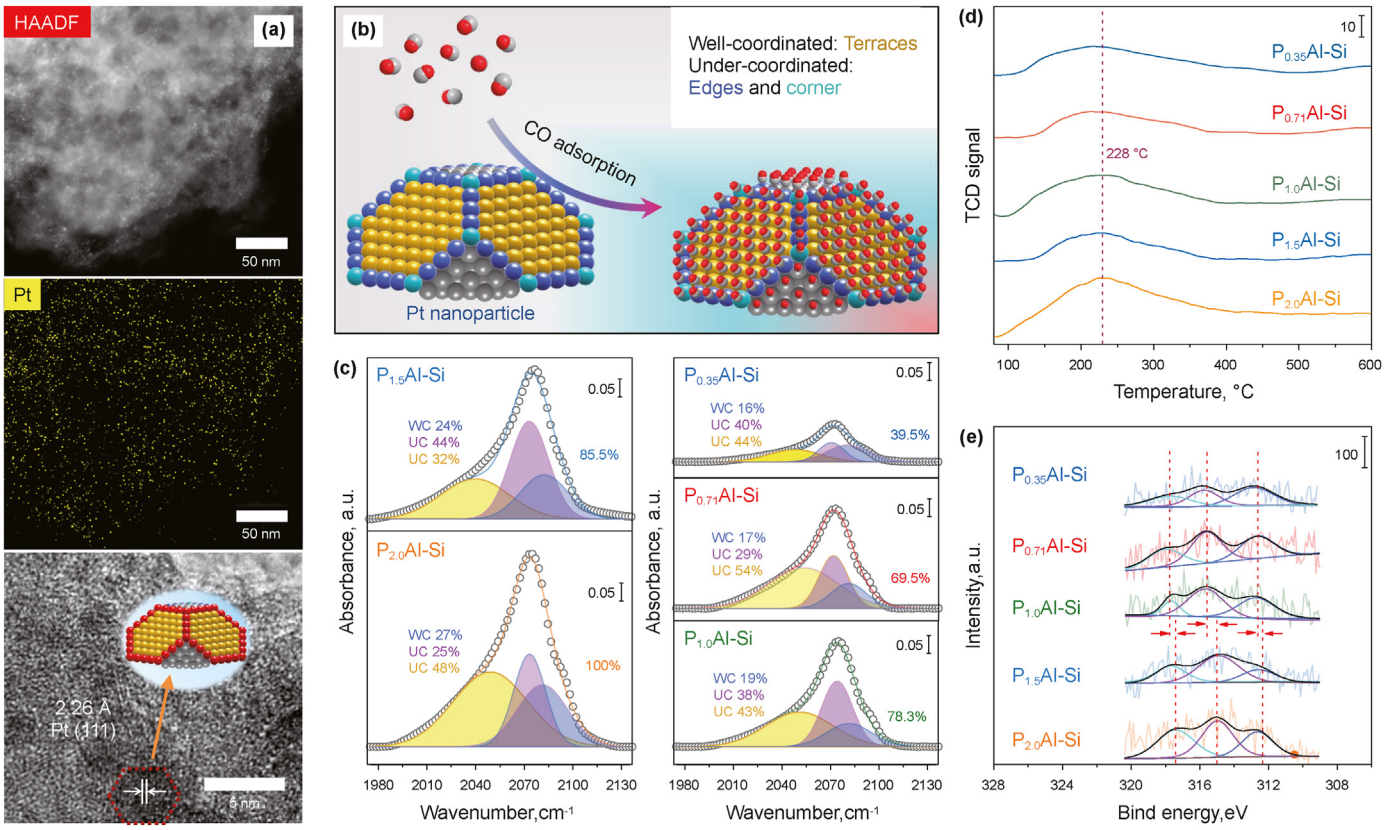

Fig. 2. **(a)** HAADF, EDX mapping and HRTEM of $P_{0.71}$Al-Si catalyst. **(b)** Schematic diagram of CO adsorbed on sites with different coordination. **(c)** DRIFTS spectra of CO adsorbed on catalysts. **(d)** H_2-TPR profiles of catalysts. **(e)** Fitting curves of the XPS peaks of Pt 4d5/2 on catalysts.

in Fig. 2(e). Each energy spectrum can be deconvoluted into three parts corresponding to Pt^{4+}, Pt^{2+} and Pt^0 species, locating at binding energy of 317.3–317.9, 314.9–315.7 and 312.3–312.8 eV, severally. The detailed bind energy and surface Pt/Al content were summarized in Table S1. The ratio of Pt/Al on the surface of catalysts increased with the enhanced Pt loading. Interestingly, the bind energy for three Pt states of $P_{0.35}$Al-Si, $P_{0.71}$Al-Si and $P_{1.0}$Al-Si shift to higher value compared with $P_{1.5}$Al-Si and $P_{2.0}$Al-Si. This can be explained by that the interaction between Pt species (PtO_x and Pt^0) on the surface and support weaken with increased Pt particle size (Zhang et al., 2020). Due to the interaction, the electron of metal Pt transferring to the support formed positively charged $Pt^{\delta+}$, which is beneficial to dehydrogenation (Tuo et al., 2021). These characterizations provide convincing evidence that the active site type and electronic state of Pt NPs on the catalyst with low loading is more favorable to dehydrogenation selectivity in contrast to high-loading catalyst. However, CO chemisorption and CO-DRIFTS characterizations demonstrated that the number of active Pt sites (C_M) increases with the enhanced loading content and the values are listed in Table 2. Apart from the active Pt sites, acidity is another crucial factor, especially strong acid sites, influencing the catalytic cracking behavior, being discussing later.

3.3. Insights into the acidity of catalysts

To get insights into acidity of Pt/Al-Si catalysts, the NH_3-TPD profiles are presented in Fig. 3(a). There are two well-resolved peaks at 100–400 °C and above 400 °C, respectively, assigned to the weak and strong acid sites (Zhang et al., 2020). The specific amount of weak (C_{WA}) and (C_{SA}) acid sties for catalysts is calculated by fitting the NH_3 desorption peaks, peaks I and II are attributed to weak acids and peak III to strong acids, and the results are listed in Table 2. The variation of total acid site amount (C_A), consistent with C_{SA} and acid site density basically is that the amount gradually declines with increased Pt loading. Strangely, the C_{WA}, C_{SA} and C_A of $P_{1.5}$Al-Si are slightly lower than that of $P_{2.0}$Al-Si, possibly caused by Pt selective occupation on the acid sites. It seems that the gap of acid site amount (C_A and acid site density) between the different catalysts is relatively little. The acidity of SiO_2-Al_2O_3 composite oxide derives from Al species rather than Si due to the absence of outer empty orbital and H atom (balance structural charge) on the Si (Pieta et al., 2010). Hence, the acid property is considerably dependent on different coordination modes, including AlO_2, AlO_3, H [AlO_4], H_2 [AlO_5] and H_3 [AlO_6], on account of various hybridization forms of Al atom outer orbitals. Three-coordinated AlO_3 and four-coordinated H [AlO_4] structures as representative Lewis (L) and Brønsted (B) acid sites respectively were schematically described in Fig. 3(b). The B acid site on the surface of four-coordinated Al is the active bridged hydroxyl (–OH) which can provide a proton to reactant. At the same time, dehydroxylation of H [AlO_4] transform to unsaturated cationic L acid site AlO_3 (electron acceptor), which can despoil the electron of reactant. The active metal component would consume the B acid site H^+ on $[AlO_4]^-$ after metal deposition, exhibiting electron-deficient $Pt^{\delta+}$ (Gao et al., 2015). Kwak et al. (2009) also have declared that Pt species can anchors on the coordinatively unsaturated Al sites. Thus, the acidity decrease with increased Pt loading is on account of occupation on acid sites by Pt.

To further test the thermal stability of B and L acid sites, *in situ* DRIFTS of adsorbed NH_3 spectrums from 100 to 350 °C were acquired and presented in Fig. 3(c). The bands at 1175, 1330 and 1625 cm^{-1} are assigned to the asymmetric and symmetric N–H

Table 2
Quantitative results of surface acid sites and average carbon deposition ($\overline{M_c}$) for catalysts.

Samples	Acid sites, mmol NH_3/g[a]			Acid site density, μmol NH_3/m^2[c]	C_M, μmol/g	C_M/C_{SA}	C_M/C_A	$\overline{M_c}$, mg/cm^2
	C_{WA}	C_{SA}	C_A					
$P_{0.35}$Al-Si	0.630	0.294 (31.8%)[b]	0.924	6.05	7.24	0.0246	0.0078	18.75
$P_{0.71}$Al-Si	0.700	0.206 (22.2%)	0.906	5.72	14.08	0.0683	0.0155	23.09
$P_{1.0}$Al-Si	0.698	0.145 (17.2%)	0.843	5.31	18.18	0.1256	0.0216	22.03
$P_{1.5}$Al-Si	0.655	0.078 (10.2%)	0.733	4.90	25.28	0.3243	0.0345	28.39
$P_{2.0}$Al-Si	0.694	0.080 (10.3%)	0.774	4.82	31.96	0.4008	0.0413	27.53

[a] C_{WA} is the sum of peaks I and II, and C_{SA} is peak III.
[b] Value in parenthesis presents the percentage of strong acid sites.
[c] Acid site density = adsorbed NH_3/specific surface area.

bending vibration of NH_3 adsorbed on the L acid sites, and that at 1455 and 1685 cm^{-1} are attributed to asymmetric and symmetric N–H bending vibration of NH_4^+ linked to the B acid sites (Auepattana-aumrung et al., 2021). However, *in situ* DRIFTS of adsorbed NH_3 cannot accurately quantify the amount of B and L acid sites. Here, the variation of corresponding peak area with temperature determines the strength of B and L acid sites. The integrated peak area for each temperature is depicted in Fig. 3(d). It is notable that the intensity of peak ascribed to the B acid site (Fig. 3(d2)) drops sharper than that belong to L acid sites (Fig. 3(d1)) with the increased temperature, demonstrating that the NH_3 species linked to the L acid sites is more difficult to desorb than that attached to B acid sites. After metal loading, the specific effect of metal sites on the *in-situ* DRIFTS of adsorbed NH_3 peak intensity of B acid and L acid sites has not been thoroughly studied, so it is difficult to explain the reasons for the change trend in this paper. The ratio (C_M/C_{SA}) of the number of active Pt sites (dehydrogenation) to the amount of strong acid sites (C–C fracture) is presented in Table 2. Without doubt, the C_M/C_{SA} and C_M/C_A increased with increasing Pt loading due to enhancement of C_M and basically constant C_A.

3.4. Cracking activity of Pt/Al-Si

Catalytic cracking performance, expressed as chemical heat sink and gas yield, for catalysts with different loading was compared in Fig. 4(a). Thereinto, the chemical heat sink was obtained by total heat sink deducting the physical heat sink, which is acquired by SUPERTRAPP procedure of NIST. The change of chemical heat sink is closely related to the variation of gas yield. It is obvious that the chemical heat sink and gas yield increased with the temperature. Particularly, the increment of chemical heat sink and gas yield is faster when the temperature reaches 650 °C. This is because of liquid cracking products further cracking into micromolecular gas products, indicating that the initial cracking temperature of liquid cracking products is about 650 °C. The reactor is the catalytic coating tube with inner diameter of 2 mm and the mass flow rate is large flow velocity of 1 g/s, so that the catalysis occurs on the inner wall of the tubular reactor and the main body of the fluid is still thermally cracked. The chemical heat sink and gas yield for *n*-decane cracking with these catalysts enhanced vastly in contrast to thermal cracking, especially at high temperatures, indicating that the addition of catalyst boost the cracking reaction depth. At 750 °C, the chemical heat sink and gas yield changed in the order of $P_{2.0}$Al-Si (1.801 MJ/kg, 78.2%) ≈ $P_{1.5}$Al-Si (1.811 MJ/kg, 79.0%) ≈ $P_{1.0}$Al-Si (1.75 MJ/kg, 78.5%) > $P_{0.71}$Al-Si (1.678 MJ/kg, 75.5%) > $P_{0.35}$Al-Si (1.546 MJ/kg, 72.7%) > TC (1.402 MJ/kg, 67.1%), and TC represents thermal cracking without adding catalyst. Nevertheless, there is no significant increase in the gas yield of *n*-decane cracking basically when the Pt loading content reaches 1.0 wt%. As the increase of metal sites and the decrease of acid sites, dehydrogenation is more obvious during the cracking process, but the gas yield changed scarcely, because the gas yield is calculated according to the mass fraction of residual liquid and dehydrogenation obviously has little effect on it.

Although products of hydrocarbon fuel cracking under high temperature is too complicated to analyze, they are still presented in Fig. 4 to provide as a reference. The components of catalytic cracking residual liquid were classified into five categories, olefins, aromatics, cycloalkanes, *i*-paraffins and others, as shown in Fig. 4(b). It is obvious that the mass fraction of olefins and aromatics raised with elevated temperature while the mass fraction of others decreased. The aromatics were regarded as one kind of chromatographically detectable coking precursor. And the typical photos of residual liquid under corresponding temperature are shown in Fig. 4(b1). Clearly, with the temperature elevating, the color of liquid changes from transparent to dark brown, which is due to enhancive content of coking precursor. Average amount of coke for different catalysts was listed in Table 2. The $\overline{M_c}$ of thermal cracking is 12.43 mg/cm^2. In contrast, the $\overline{M_c}$ over these catalytic coating is more than that over bare tube, which is related to the that the higher cracking depth is accompanied with coking and the active sites (metal and acid) would result in coking side reaction. The $\overline{M_c}$ increased with gas yield increase when the C_M/C_{SA} below 0.13. The carbon deposition (22.03 mg/cm^2) and activity reached balance at C_M/C_{SA} of 0.13, while the carbon deposition increased at C_M/C_{SA} above 0.13 due to deep dehydrogenation coking.

It is known from the literatures (Zhou et al., 2014) that the content of hydrogen and alkenes in the gas phase products is closely related to the heat sink and the amount of coking during fuel cracking reaction. Fig. 4(c) and (d) showed that the changing trend diagram of the relationship between gas yield of each catalyst and selectivity of target products (alkenes/H_2 selectivity). In this work, alkenes selectivity of gaseous products was indexed as the ratio of alkenes and hydrogen to alkanes (ene + H_2/ane). The alkenes selectivity first increases severely and then decreases slightly with the gas yield (or the reaction temperature), as depicted in Fig. 4(c). Alkenes and hydrogen main derive from β-scission and dehydrogenation reaction, indicating that the corresponding fraction increase when the secondary reaction occurs at high gas yield. Meantime, there is no clear variation regularity of the ene + H_2/ane among different catalysts due to commixture of thermal and catalytic cracking products in the mini-channel coating reactor. In addition, the H_2 selectivity of different catalysts are shown in Fig. 4(d), which first sharply decrease and then decrease slightly with the gas yield (or the reaction temperature), and the lowest H_2 selectivity reached about 2.5% at 650 °C. This trend is mainly due to the C–H bond of *n*-decane breakage occurs mainly on the catalysts surface at 600 °C, while the C–C and C–H bond breakage occurs simultaneously at 650 °C and above 650 °C. The proportion of C–H bond breakage decreases and then tends to be stable as the temperature gradually increases, so the H_2 selectivity appears a low

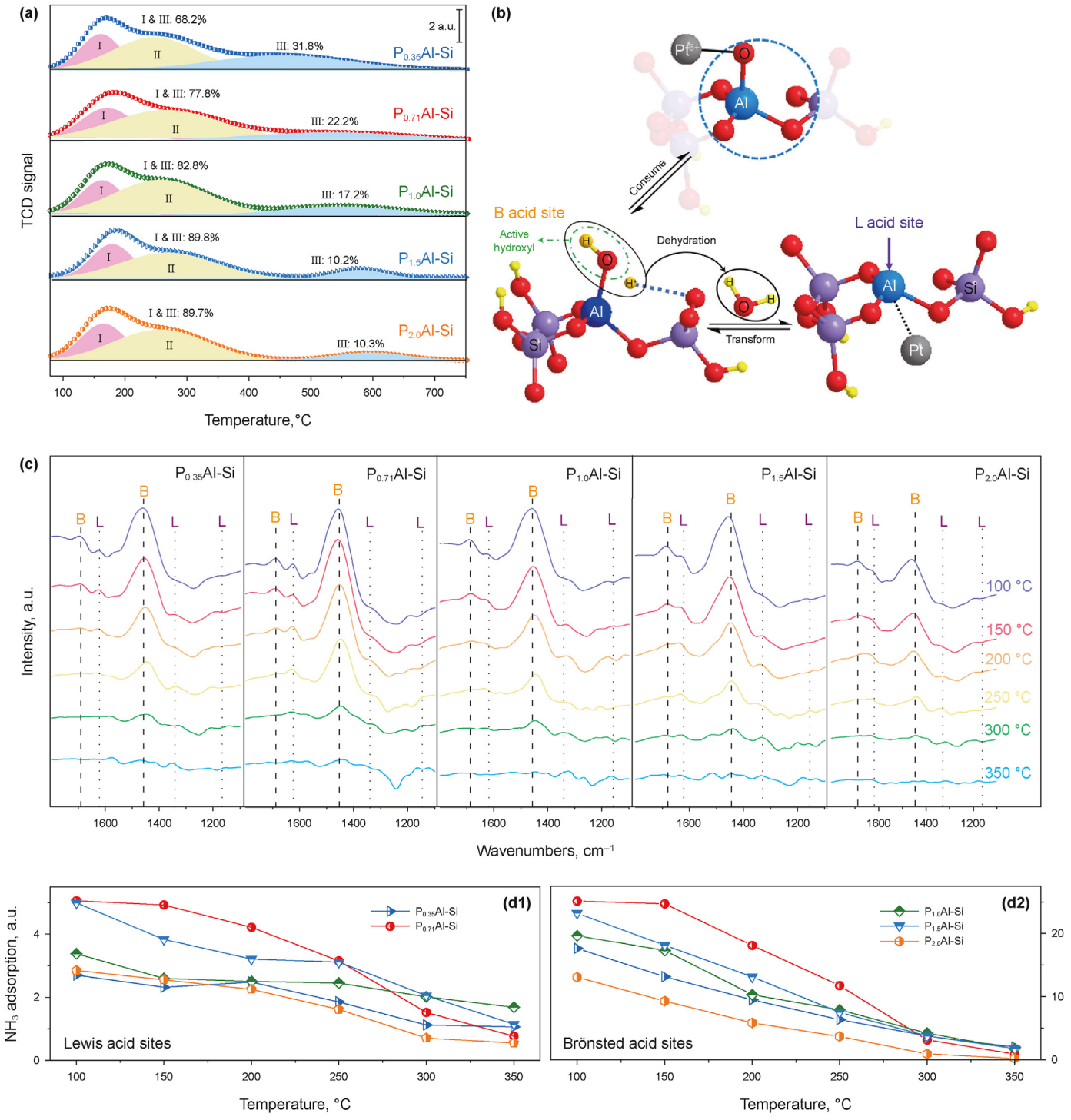

Fig. 3. **(a)** NH_3-TPD profiles for the Pt/Al-Si catalysts. **(b)** Schematic diagram for acid sites states on the surface of Pt/Al-Si catalysts. **(c)** *In situ* DRIFTS of adsorbed NH_3 spectrums for catalysts. **(d)** Relative intensity of L (d1) and B (d2) acid sites.

point at 650 °C and then slightly increases.

4. Effect of metal-acid sites balance and corresponding mechanism

The balance between dehydrogenation and C–C fracture function was estimated by the ratio of active Pt metal sites to strong acid sites (C_M/C_{SA}), as demonstrated in Table 2. The monofunctional cracking catalysts in our previous work can be regard as a reference (Hou et al., 2018). On the one hand, Pt supported alkaline MgO catalyst with only metallic sites exhibited the worse cracking activity in contrast to Pt supported acidic oxides, such as weakly acidic SiO_2 (0.33 mmol NH_3/g). On the other hand, the SiO_2-Al_2O_3 with only acid sites (0.52 mmol NH_3/g) contributes to lower *n*-decane cracking activity than 0.71 wt% Pt loaded SiO_2-Al_2O_3. In this work, to correlate the C_M/C_{SA} with catalytic cracking performance,

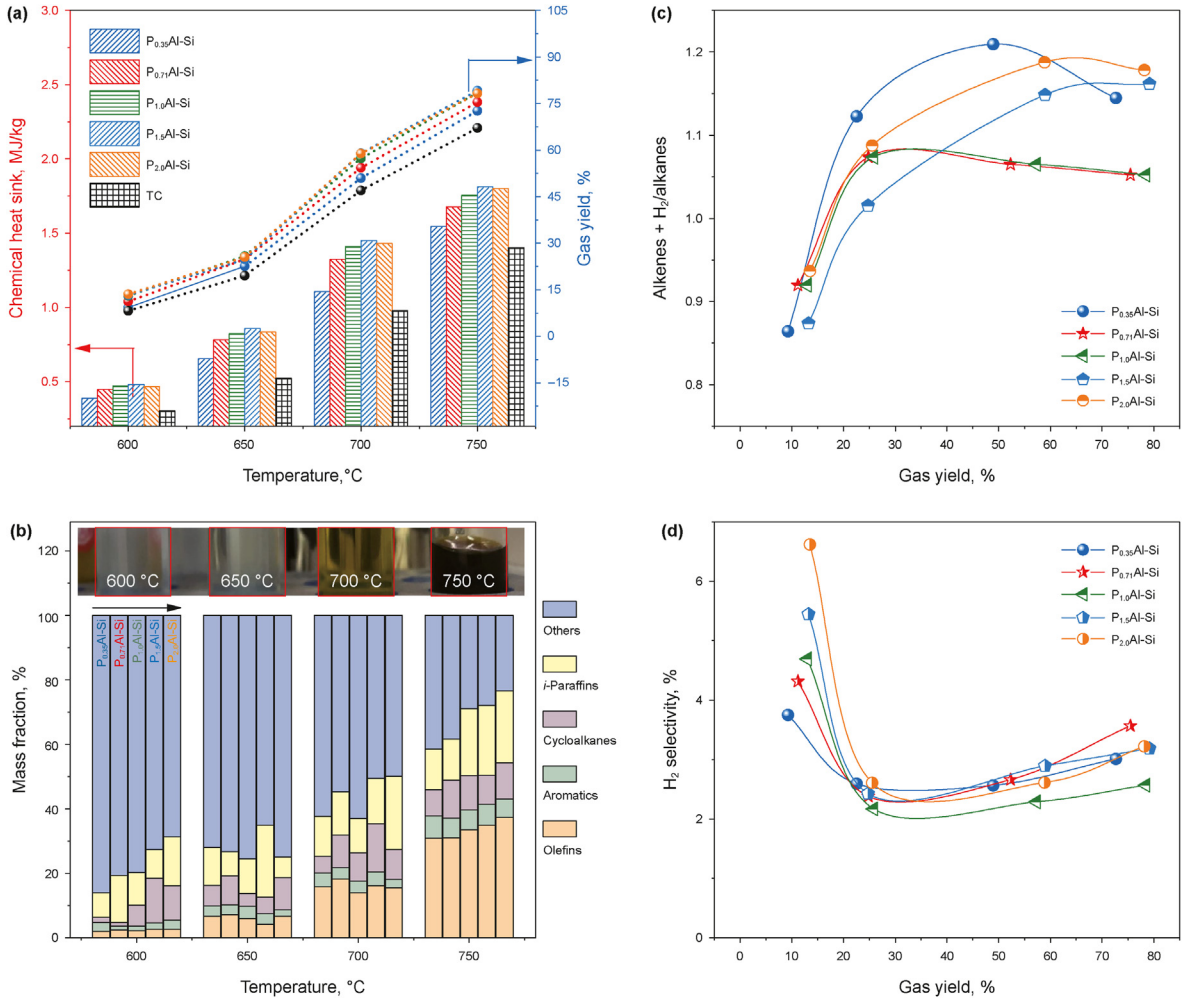

Fig. 4. **(a)** Chemical heat sink and gas yield for catalysts under different temperatures. **(b)** Mass fraction of olefins, aromatics, cycloalkanes and *i*-paraffins in the liquid products. **(c)** The ratio of alkenes + H_2/alkanes in gaseous products for different catalysts. **(d)** H_2 selectivity in gaseous products vs. gas yield for different catalysts.

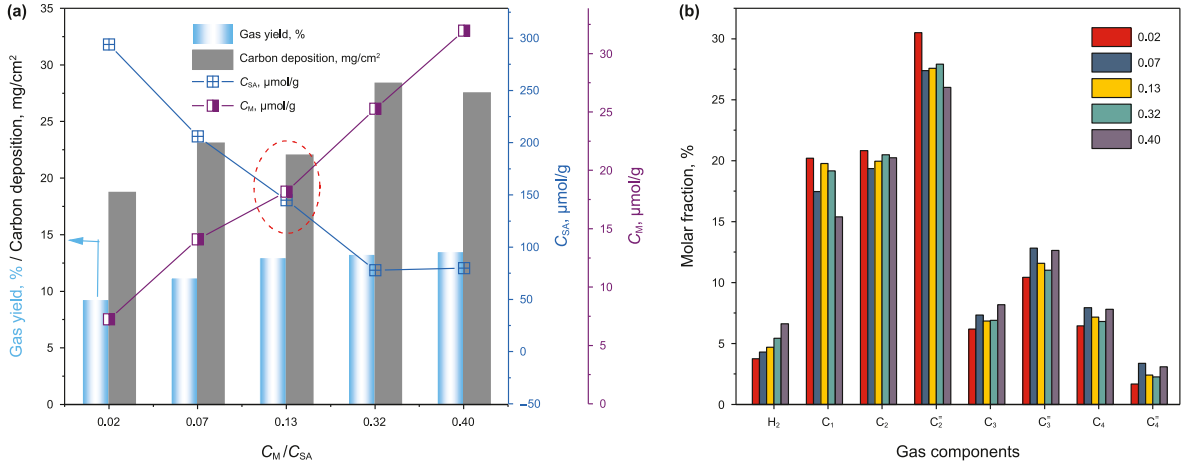

Fig. 5. Effect of metal-acid sites balance on the gas yield **(a)** and gas product distribution **(b)** at 600 °C over Pt/Al-Si catalyst with different C_M/C_{SA}.

gas yield of *n*-decane cracking at 600 °C over dual-sites catalysts as a function of C_M/C_{SA} was provided in Fig. 5(a). Actually, the contribution of catalytic cracking to gas yield at low temperature is greater than that at high temperature. At the same time, the primary cracking of *n*-decane occurred at low temperature without products further cracking. Hence, the gas yield and products for these catalysts at 600 °C were selected to detailly discuss the metal-acid sites balance effect of dual-sites catalysts on hydrocarbon

cracking. Firstly, there was a negative correlation between the C_M and the C_{SA} that as the C_M elevating (7.24 < 14.08 < 18.18 < 25.28 < 31.96 μmol/g), the C_{SA}, drops gradually (294 > 206 > 145 > 78 ≈ 80 μmol/g). Then, the gas yield increased gradually with varied C_M/C_{SA} and reached a plateau at C_M/C_{SA} of 0.13, implying that the active Pt species play a significant role in cracking. The carbon deposition exhibited similar trend with gas yield over catalysts with different C_M/C_{SA}. When C_{SA} remained almost constant (c.a. 80 μmol NH_3/g), although C_M increased from 25.28 to 31.96 μmol/g, the gas yield changed hardly. this suggests that the cracking activity cannot be enhanced through enhancing the C_M when the C_{SA} reached low value. Mentioned change trend is consistent with the traditionally dual-sites catalysts for hydroisomerization (Jiao et al., 2020), which can be explained by that the reaction rate was limited by the Pt metal sites at low C_M/C_{SA} and strong acid sites at high C_M/C_{SA}. Thus, both the number of metal sites and strong acid sites of dual-sites catalysts are important, and either higher or lower is not appropriate. Only when the proportion (C_M/C_{SA}) reaches a balance (0.13), the dual-sites catalyst can function to the greatest extent and reduce the cost. In addition, the effect of textural properties as well as Pt particle size of a series of dual-sites Pt/Al-Si catalysts on hydrocarbon cracking can be ignored according to the above discussion.

To further investigate the effect of electronic state of metal sites and metal-acid sites balance on cracking reaction pathway, the gaseous product distribution at 600 °C was analyzed, as listed in Fig. 5(b). The gaseous products primarily consist of hydrogen (H_2), methane (C_1), ethane (C_2), ethylene ($C_2^=$), propane (C_3), propene ($C_3^=$), butane (C_4) and butene ($C_4^=$). Thereinto, C_1, C_2 and $C_2^=$ are the main products and molar fraction is higher than 15%. The conversion of *n*-decane cracking under low temperature (600 °C) is relatively low, so the cracking pathway is unimolecular proton cracking rather than bimolecular reaction and side reactions. The possible cracking pathways for small molecule gaseous products (≤C4) of *n*-decane cracking over dual-sites Pt/Al-Si catalyst are presented in Fig. 6. Here, *n*-decane molecule obtains proton from the strong acid site to generate pentacoordinated carbenium ($C_{10}H_{23}^+$). Normally, carbenium can form on different carbon (C) of *n*-decane molecule (*n*-$C_{10}H_{22}$), but it is easier to form secondary carbenium than primary carbenium. The detailed cracking process is as follows:

(1) Protolytic cracking (ProC): Unimolecular proton cracking of the reaction a–e in Fig. 6 can generate H_2, C_1, C_2, C_3, C_4 molecules and corresponding tricoordinated $C_{10}H_{21}^+$, $C_9H_{19}^+$, $C_8H_{17}^+$, $C_7H_{15}^+$, $C_6H_{13}^+$ carbenium, which would further crack into $C_3H_7^+$ and $C_4H_9^+$ carbenium. One pathway is that hydrogen transfer (H-tran) reaction between the above carbenium and *n*-$C_{10}H_{22}$ to produce new tricoodinated $C_{10}H_{21}^+$ carbenium and corresponding alkanes (C_3 and C_4). Another pathway is deprotonation reaction that generate $C_3^=$ and $C_4^=$ alkenes and recover B acid sites.

(2) *β*-scission (*β*-Sci): Pentacoordinated $C_{10}H_{23}^+$ carbenium may undergo *β*-scission of the reaction f–h in Fig. 6, that is, the C–C bond between *β*–C and ionic carbon (*α*–C) breaks into $C_2^=$, $C_3^=$ and $C_4^=$ alkene molecules and $C_8H_{17}^+$, $C_7H_{15}^+$, $C_6H_{13}^+$ carbenium, respectively, and these carbenium would undergo the reaction in Eq. (1).

(3) Dehydrogenation (Dehy): Two adjacent carbons (C) of *n*-$C_{10}H_{22}$ are adsorbed by Pt sites on the catalyst, and their C–H bonds are activated and broken, then, hydrogen (H_2) is obtained by mutual bonding of two H atoms. On the one hand, the removal of the H atoms forms a double bond between the two C atoms and the H atom on the secondary carbon is more likely to be removed than the H atom on the primary carbon to produce 2-decene. If both *n*-decane and 2-decene are near the strong acid site on the catalyst, the 2-decene molecule is more likely to form carbenium, this would reduce the reaction energy barrier for the rate-determining step (carbenium formation), which is one of the main ways to improve cracking activity of *n*-decane on a bicenter catalyst. On the other hand, the C–C bond between the two C atoms after the removal of H atoms continue to be activated and broken on Pt sites to produce $C_2^=$ and $C_8H_{16}^=$ alkenes. In addition, oligomerization, isomerization, cyclization, aromatization, dehydrogenation and other side reactions of carbon deposition are not described here.

Each cracking gas phase product is linked to one or several reaction pathways, and it is difficult to calculate the contribution of reaction pathways to the final gas phase product distribution. However, it is possible to make a qualitative analysis of the reaction pathway. Hou et al. (2017a) have investigated that reaction mechanism for *n*-hexane cracking on HZSM-5 zeolite catalyst, found that cracking products can reflect the relative activity of C–C bond or C–H fracture on the catalyst. It is also found that the approximate order of C–C or C–H bonds break is $^{3\#}C–^{4\#}C$ (C_3, $C_3^=$) > C–H (H_2, $C_3^=$) > $^{2\#}C–^{3\#}C$ (C_2, $C_4^=$) > $^{3\#}C–^{2\#}C$ ($C_2^=$, C_4) > $^{1\#}C–^{2\#}C$ (C_1, $C_5^=$). It can be seen from Fig. 5(b) that the relative content sequence of gaseous products from *n*-decane cracking is $C_2^=$ > C_2 ≈ C_1 > $C_3^=$ > C_3 ≈ C_4 > H_2 > $C_4^=$. Through the theoretical analysis of the above reaction pathways, some basic reaction pathways of *n*-decane cracking into gaseous products are summarized in Table 3. The relative content of alkenes is higher than that of alkanes among the molecules with carbon number of 1, 2 and 3 in the gaseous products. This indicates that the reaction rate of *β*-Sci and low-carbon carbenium deprotonation is faster than that of unimolecular proton cracking and low-carbon carbenium H-transfer. C_2 alkane is formed by proton cracking with the elimination of the $^{2\#}C–^{3\#}C$ bond and C_1 alkane is formed by proton cracking with the elimination of the $^{1\#}C–^{2\#}C$ bond. There is no C_1^+ and C_2^+ hydrogen transfer reaction due to high energy barrier. Combined with the gas phase products distribution, it can be inferred that the active order of C–C bond or C–H bond elimination reaction is $^{2\#}C–^{3\#}C$ > $^{1\#}C–^{2\#}C$ > $^{3\#}C–^{4\#}C$ > $^{4\#}C–^{5\#}C$ > C–H.

It can be seen from Fig. 6 that the H_2 is produced by dehydrogenation of the active metal Pt sites and unimolecular proton cracking on the strong acid sites. The relative content of H_2 increases with the augmentation of metal-to-strong acid sites ratio (C_M/C_{SA}). However, there is no significant difference in the relative content of H_2 under each C_M/C_{SA}. On the one hand, when C_M/C_{SA} is low, there are more strong acid sites on the catalyst, leading to increase in the proportion of $C_{10}H_{22}$ cracking into C_{10}^+ and H_2 by unimolecular proton cracking. At the same time, the small size of Pt nanoparticles, high proportion of UC sites and partial positive charge $Pt^{\delta+}$ on the surface of the catalyst are favorable for dehydrogenation, but the number of active metal sites is insufficient. On the other hand, when C_M/C_{SA} is high, the number of active metal sites for dehydrogenation is abundant, but the chemical state of Pt nanoparticles is less favorable and H_2 production is little by unimolecular proton cracking at strong acid sites. In general, the content of H_2 increases with the increase of C_M/C_{SA}, indicating that the number of active metal Pt sites on the catalyst surface is the main factor affecting the dehydrogenation activity, followed by the chemical state of Pt.

When C_M/C_{SA} is 0.02, the relative content of C_1, C_2, and $C_2^=$ in the gas phase is basically the highest, but H_2 is the least, which is due to the largest number of strong acid sites on the catalyst, the $^{2\#}C–^{3\#}C$ bond and $^{1\#}C–^{2\#}C$ bond elimination unimolecular proton cracking and *β*-Sci continue to occur. With the increase of C_M/C_{SA}, the relative content of C_1, C_2, and $C_2^=$ first decrease and then increase, the

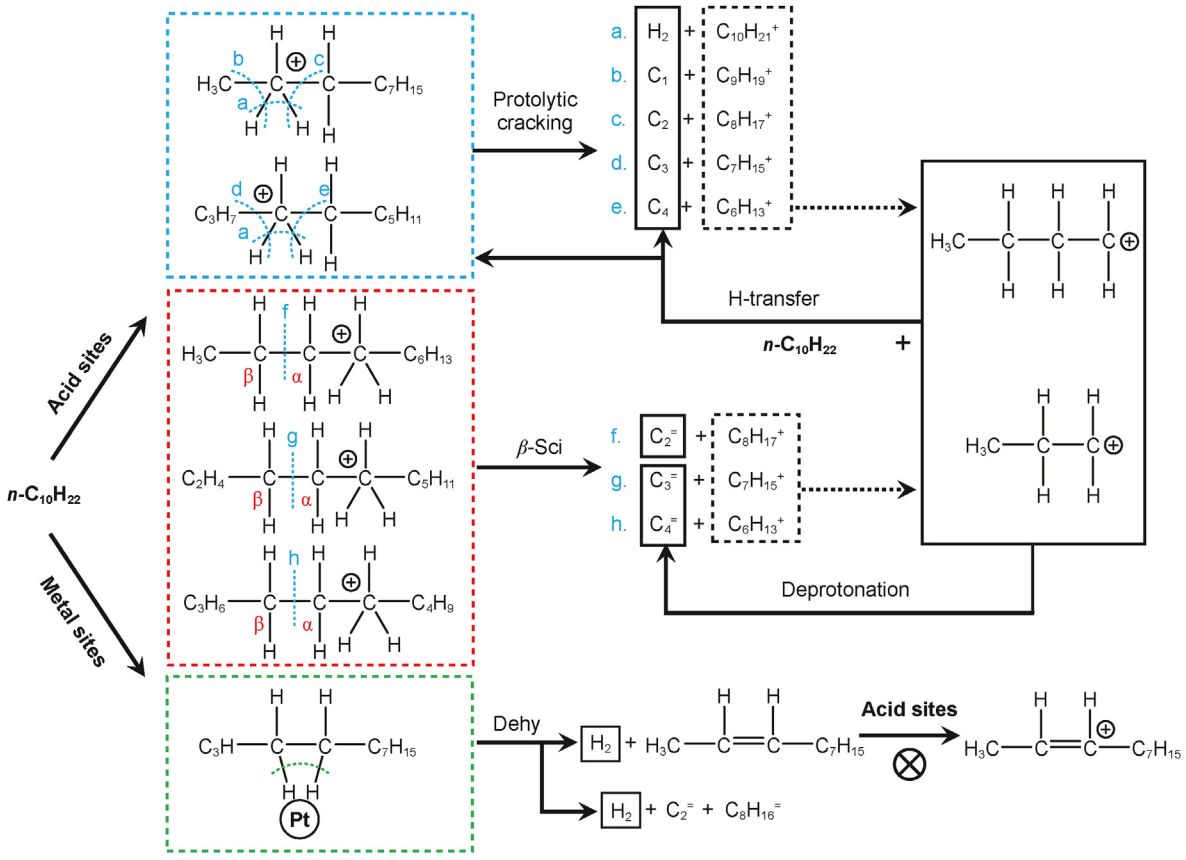

Fig. 6. The possible pathways of *n*-decane cracking reaction over dual-sites Pt/Al-Si catalyst.

Table 3
Possible reaction pathways for *n*-decane cracking at 600 °C over Pt/Al-Si catalyst.

Product	Reaction pathway	Product	Reaction pathway
$C_2^=$	$C_{10}^+ \rightarrow C_8^+ + C_2^=$ (β-Sci)	C_4	$C_{10}^+ \rightarrow C_6^+ + C_4$ (ProC)
C_2	$C_{10}^+ \rightarrow C_8^= + C_2^= + H_2$ (Dehy)		$C_4^+ + C_{10} \rightarrow C_{10}^+ + C_4$ (H-tran)
	$C_{10}^+ \rightarrow C_8^+ + C_2$ (ProC)	H_2	$C_{10}^+ \rightarrow C_8^= + C_2^= + H_2$ (Dehy)
C_1	$C_{10}^+ \rightarrow C_9^+ + C_1$ (ProC)		$C_{10}^+ \rightarrow C_{10}^+ + H_2$ (ProC)
$C_3^=$	$C_{10}^+ \rightarrow C_7^+ + C_3^=$ (β-Sci)	$C_3^=$	$C_{10}^+ \rightarrow C_6^+ + C_4^=$ (β-Sci)
	$C_3^+ \rightarrow C_3^=$ (Deprotonation)		$C_4^+ \rightarrow C_4^=$ (Deprotonation)
C_3	$C_{10}^+ \rightarrow C_7^+ + C_3$ (ProC)		
	$C_3^+ + C_{10} \rightarrow C_{10}^+ + C_3$ (H-tran)		

possible reasons are speculated as follows: when C_M/C_{SA} is 0.07, the number of strong acid sites decreased by 88 μmol/g, which slow the rate of unimolecular proton cracking and β-Sci for elimination of $^{2\#}C-^{3\#}C$ bond and $^{1\#}C-^{2\#}C$ bond, even though the metal sites increased by 6.84 μmol/g, it could not offset the effect of the decrease of strong acid sites. When C_M/C_{SA} is 0.13, the increase of metal sites can promote the formation of 2-decene molecules, and the formation of alkylene carbenium is easier to boost the reaction for production of C_1, C_2, and $C_2^=$. When C_M/C_{SA} continues to increase, the number of strong acid sites decreases to about 80 μmol/g. Even if the number of metal sites increases, the reaction rate for production of C_1, C_2, and $C_2^=$ decrease, this is similar to the variation of *n*-decane conversion with C_M/C_{SA} of dual-sites catalyst.

5. Conclusion

In this work, the impact of metal-acid sites balance over Pt/Al-Si dual-sites catalysts on efficient cracking of supercritical *n*-decane was investigated via changed Pt loading. The balance results of high heat sink of *n*-decane cracking and carbon deposition from deep dehydrogenation over catalyst over appropriate metal-acid sites was obtained by regulating C_M/C_{SA}. The amount of strong acid sites decreases with the increase of Pt loading due to the interaction between Pt species and surface acid groups. when C_M/C_{SA} is 0.13, the chemical heat sink is 1.75 MJ/kg and average carbon deposition is 22.03 mg/cm^2. The gas phase products and cleavage reaction pathway were analyzed in detail, and the sequence of C—C or C—H bond elimination reaction was deduced that is $^{2\#}C-^{3\#}C > {}^{1\#}C-^{2\#}C > {}^{3\#}C-^{4\#}C > {}^{4\#}C-^{5\#}C >$ C—H. Additionally, a quantitative correlation between the metal-acid sites balance and catalytic cracking activity was built.

Declaration of competing interest

The authors declare that they have no known competing financial interests or personal relationships that could have

appeared to influence the work reported in this paper.

CRediT authorship contribution statement

Liu-Ling Chen: Writing – review & editing, Writing – original draft, Visualization, Methodology, Investigation, Formal analysis, Conceptualization. **Jun Zhang:** Writing – review & editing, Conceptualization. **Chun-Guang Li:** Formal analysis. **Li-Qun Fei:** Writing – review & editing, Formal analysis. **Bo Wang:** Writing – review & editing, Investigation, Formal analysis. **Chen-Qi Zhang:** Writing – review & editing, Investigation, Formal analysis. **Yi Jiao:** Writing – review & editing, Funding acquisition, Conceptualization. **Jian-Li Wang:** Project administration, Conceptualization.

Acknowledgements

This work was subsidized by Sichuan Province Science and Technology Program (2023NSFSC0093) and Enterprises Entrust Technology Development Program (FJF22KX0055, 202302914).

Appendix A. Supplementary data

Supplementary data to this article can be found online at https://doi.org/10.1016/j.petsci.2024.02.005.

References

Auepattana-aumrung, C., Praserthdam, S., Wannakao, S., et al., 2021. Observation of reduction on alkane products in butene cracking over ZSM-5 modified with Fe, Cu, and Ni catalysts. Fuel 291, 120265. https://doi.org/10.1016/j.fuel.2021.120265.

Chen, W.Y., Zheng, W.Z., Cao, J.B., et al., 2020. Atomic insights into robust Pt-PdO interfacial site-boosted hydrogen generation. ACS Catal. 10, 11417–11429. https://doi.org/10.1021/acscatal.0c03214.

Chen, F.Q., Hao, J., Yu, Y.Y., et al., 2022. The influence of external acid strength of hierarchical ZSM-5 zeolites on n-heptane catalytic cracking. Microporous Mesoporous Mater. 330, 111575. https://doi.org/10.1016/j.micromeso.2021.111575.

Chen, K., Zhao, J.Y., Li, A.H., et al., 2022. Realumination of dealuminated HZSM-5 zeolites by acid treatment, the impact of AlF distribution and its catalytic cracking performance of alkanes. Microporous Mesoporous Mater. 338, 111969. https://doi.org/10.1016/j.micromeso.2022.111969.

Dong, X.L., Shaikh, S., Vittenet, J.R., et al., 2018. Fine tuning the diffusion length in hierarchical ZSM-5 to maximize the yield of propylene in catalytic cracking of hydrocarbons. ACS Sustainable Chem Eng 6, 15832–15840. https://doi.org/10.1021/acssuschemeng.8b04441.

Feng, Y., Liu, Y.N., Cao, Y., et al., 2020. Thermal management evaluation for advanced aero-engines using catalytic steam reforming fo hydrocarbon fuels. Energy 193, 116738. https://doi.org/10.1016/j.energy.2019.116738.

Gao, J., Zheng, Y.T., Jehng, J.M., et al., 2015. Identification of molybdenum oxide nanostructures on zeolites for natural gas conversion. Science 348, 686–690. https://doi.org/10.1126/science.aaa7048.

Hammer, B., Nielsen, O.H., Nrskov, J.K., 1997. Structure sensitivity in adsorption: CO interaction with stepped and reconstructed Pt surfaces. Catal. Lett. 46, 31–35. https://doi.org/10.1023/A:1019073208575.

Hou, X., Qiu, Y., Zhang, X.W., et al., 2017a. Analysis of reaction pathways for n-pentane cracking over zeolites to produce light olefins. Chem Eng J 307, 372–381. https://doi.org/10.1016/j.cej.2016.08.047.

Hou, X., Qiu, Y., Zhang, X.W., et al., 2017b. Effects of regeneration of ZSM-5 based catalysts on light olefins production in n-pentane catalytic cracking. Chem Eng J 321, 572–583. https://doi.org/10.1016/j.cej.2017.03.127.

Hou, X., Qiu, Y., Tian, Y.J., et al., 2018. Reaction pathways of n-pentane cracking on the fresh and regenerated Sr, Zr and La-loaded ZSM-5 zeolites. Chem Eng J 349, 297–308. https://doi.org/10.1016/j.cej.2018.05.026.

He, X.Y., Tian, Y.J., Qiao, C.Z., et al., 2023. Acid-driven architecture of hierarchical porous ZSM-5 with high acidic quantity and its catalytic cracking performance. Chem Eng J 473, 145334. https://doi.org/10.1016/j.cej.2023.145334.

Jiao, Y., Chen, T., Wang, L.L., et al., 2020. Synthesis of a high-stability nanosized Pt-loaded $MgAl_2O_4$ catalyst for n-Decane cracking with enhanced activity and durability. Ind. Eng. Chem. Res. 59, 4338–4347. https://doi.org/10.1021/acs.iecr.9b06515.

Kwak, J., Hu, J.Z., Mei, D.H., et al., 2009. Coordinatively unsaturated Al^{3+} centers as binding sites for active catalyst phases of Platinum on γ-Al_2O_3. Science 325, 1670–1673. https://doi.org/10.1126/science.1176745.

Kim, S., Sasmaz, E., Lauterbach, J., 2015. Effect of Pt and Gd on coke formation and regeneration during JP-8 cracking over ZSM-5 catalysts. Appl. Catal. B Environ. 168–169, 212–219. https://doi.org/10.1016/j.apcatb.2014.12.027.

Kale, M.J., Christopher, P., 2016. Utilizing quantitative in situ FTIR spectroscopy to identify well-coordinated Pt atoms as the active site for CO oxidation on Al_2O_3-supported Pt catalysts. ACS Catal. 6, 5599–5609. https://doi.org/10.1021/acscatal.6b01128.

Ludwig, J., Vlachos, D.G., Van Duin, A.C.T., et al., 2006. Dynamics of the dissociation of hydrogen on stepped Platinum surfaces using the ReaxFF reactive force field. J. Phys. Chem. B 110, 4274–4282. https://doi.org/10.1021/jp0561064.

Lundwall, M.J., McClure, S.M., Goodman, D.W., 2010. Probing terrace and step sites on Pt nanoparticles using CO and ethylene. J. Phys. Chem. C 114, 7904–7912. https://doi.org/10.1021/jp9119292.

Lee, S., Lee, S., Kumbhalkar, M.D., et al., 2017. Effect of particle size upon Pt/SiO_2 catalytic cracking of n-Dodecane under supercritical conditions: in situ SAXS and XANES studies. ChemCatChem 9, 99–102. https://doi.org/10.1002/cctc.201600829.

Lyu, Y.C., Yu, Z.M., Yang, Y., et al., 2019. Metal-acid balance in the in-situ solid synthesized Ni/SAPO-11 catalyst for n-hexane hydroisomerization. Fuel 243, 398–405. https://doi.org/10.1016/j.fuel.2019.01.013.

Long, L., Zhou, W.X., Qiu, Y.F., et al., 2020. Coking and gas products behavior of supercritical n-decane over NiO nanoparticle/nanosheets modified HZSM-5. Energy 192, 116540. https://doi.org/10.1016/j.energy.2019.116540.

McCarthy, D.N., Strebel, C.E., Johansson, T.P., et al., 2012. Structural modification of Platinum model systems under high pressure CO annealing. J. Phys. Chem. C 116, 15353–15360. https://doi.org/10.1021/jp302379x.

Musselwhite, N., Na, K., Sabyrov, K., et al., 2015. Mesoporous aluminosilicate catalysts for the selective isomerization of n-Hexane: the roles of surface acidity and platinum metal. J. Am. Chem. Soc. 137, 10231–10237. https://doi.org/10.1021/jacs.5b04808.

Mendes, P.S.F., Silva, J.M., Ribeiro, M.F., et al., 2020. Bifunctional intimacy and its interplay with metal-acid balance in shaped hydroisomerization catalysts. ChemCatChem 12, 4582–4592. https://doi.org/10.1002/cctc.202000624.

Pieta, I.S., Ishaq, M., Wells, R.P.K., et al., 2010. Quantitative determination of acid sites on silica-alumina. Appl Catal A:Gen. 390, 127–134. https://doi.org/10.1016/j.apcata.2010.10.001.

Samad, J.E., Blanchard, J., Sayag, C., et al., 2016. The controlled synthesis of metal-acid bifunctional catalysts: the effect of metal:acid ratio and metal-acid proximity in Pt silica-alumina catalysts for n-heptane isomerization. J. Catal. 342, 203–212. https://doi.org/10.1016/j.jcat.2016.08.004.

Shang, Q.H., Xu, G.L., Tang, N.F., et al., 2019. Fluoride-modified ZSM-5 for endothermic catalytic cracking of n-decane. Microporous Mesoporous Mater. 288, 109616. https://doi.org/10.1016/j.micromeso.2019.109616.

Song, K.H., Jeong, S.K., Park, K.T., et al., 2020. Supercritical catalytic cracking of n-dodecane over air-oxidized activated charcoal. Fuel 276, 118010. https://doi.org/10.1016/j.fuel.2020.118010.

Sun, H.Q., Zhang, Y.Y., Li, Y.M., et al., 2021. Synergistic construction of bifunctional and stable Pt/HZSM-5-based catalysts for efficient catalytic cracking of n-butane. Nanoscale 13, 5103–5114. https://doi.org/10.1039/D1NR00302J.

Tian, Y.J., Zhang, B.F., Gong, S.Y., et al., 2021. Synthesis of pillared nanosheet HZSM-5 zeolite films for catalytic cracking of supercritical n-dodecane. Microporous Mesoporous Mater. 310, 110598. https://doi.org/10.1016/j.micromeso.2020.110598.

Tuo, Y.X., Meng, Y., Chen, C., et al., 2021. Partial positively charged Pt in $Pt/MgAl_2O_4$ for enhanced dehydrogenation activity. Appl. Catal. B Environ. 288, 119996. https://doi.org/10.1016/j.apcatb.2021.119996.

Wang, Z.Z., Zhang, H., Li, S.S., et al., 2017. The performance of Rh/SiO_2-Al_2O_3 catalysts in methycyclohexane cracking reaction. J. Anal. Appl. Pyrol. 124, 475–485. https://doi.org/10.1016/j.jaap.2017.02.012.

Wang, W., Liu, C.J., Wu, W., 2019. Bifunctional catalysts for the hydroisomerization of n-alkanes: the effects of metal-acid balance and textural structure. Catal. Sci. Technol. 9, 4162–4187. https://doi.org/10.1039/C9CY00499H.

Xiao, X., Sun, B., Wang, P., et al., 2022. Tuning the density of Brønsted acid sites on mesoporous ZSM-5 zeolite for enhancing light olefins selectivity in the catalytic cracking of n-octane. Microporous Mesoporous Mater. 330, 111621. https://doi.org/10.1016/j.micromeso.2021.111621.

Ye, D.F., Zhao, L., Bai, S.S., et al., 2019. New strategy for high-performance integrated catalysts for cracking hydrocarbon fuels. ACS Appl. Mater. Interfaces 11, 40078–40090. https://doi.org/10.1021/acsami.9b14285.

Zhou, W., Jia, Z., Qin, J., et al., 2014. Experimental study on effect of pressure on heat sink of n-decane. Chem. Eng. J. 243, 127–136. https://doi.org/10.1016/j.cej.2013.12.081.

Zhu, Y.H., Peng, W., Xu, R.N., et al., 2018. Review on active thermal protection and its heat transfer for airbreathing hypersonic vehicles. Chin. J. Aeronaut. 31, 1929–1953. https://doi.org/10.1016/j.cja.2018.06.011.

Zhang, W., Wang, H.Z., Jiang, J.W., et al., 2020. Size dependence of Pt catalysts for propane dehydrogenation: from atomically dispersed to nanoparticles. ACS Catal. 10, 12932–12942. https://doi.org/10.1021/acscatal.0c03286.

Zhang, J., Cheng, M., Jiao, Y., et al., 2021. Enhanced cracking conversion of supercritical fuel over stabilized Pt nanoparticles supported SiO_2-Al_2O_3 catalyst coating. Appl. Surf. Sci. 559, 149950. https://doi.org/10.1016/j.apsusc.2021.149950.